

# ARCSTONE: calibration of lunar spectral reflectance from space. Prototype instrument concept, analysis, and results

Hans Courier<sup>a,\*</sup>, Rand Swanson<sup>a</sup>, Constantine Lukashin<sup>b</sup>, Christine Buleri<sup>c</sup>, John Carvo<sup>d</sup>, Michael Cooney<sup>b</sup>, Warren Davis<sup>b</sup>, Alexander Halterman<sup>c</sup>, Alan Hoskins<sup>e</sup>, Trevor Jackson<sup>b</sup>, Mike Kehoe<sup>a</sup>, Greg Kopp<sup>e</sup>, Thuan Nguyen<sup>b</sup>, Noah Ryan<sup>b</sup>, Carlos Roithmayr<sup>b</sup>, Paul Smith<sup>e</sup>, Mike Stebbins<sup>a</sup>, Thomas Stone<sup>f</sup>, and Cindy Young<sup>b</sup>

<sup>a</sup>Resonon Inc., Bozeman, Montana, United States

<sup>b</sup>NASA Langley Research Center, Hampton, Virginia, United States

<sup>c</sup>Quartus Engineering, San Diego, California, United States

<sup>d</sup>Blue Canyon Technologies LLC, Boulder, Colorado, United States

<sup>e</sup>University of Colorado, Laboratory for Atmospheric and Space Physics, Boulder, Colorado, United States

<sup>f</sup>United States Geological Survey, Flagstaff, Arizona, United States

**ABSTRACT.** The ARCSTONE project objective is to acquire accurate measurements of the spectral lunar reflectance from space, allowing the Moon to be used as a high-accuracy SI-traceable calibration reference by spaceborne sensors in low-Earth and geostationary orbits. The required spectral range is 350 to 2300 nm with 4-nm sampling. The ARCSTONE approach is to measure solar and lunar spectral irradiances with a single set of optics and determine spectrally resolved lunar reflectances via a direct ratioing method, eliminating long-term optical degradation effects. Lunar-irradiance values, derived from these direct reflectance measurements, are enabled by independently measured SI-traceable spectral solar irradiances, essentially using the Sun as an on-orbit calibration reference. In an initial attempt to demonstrate this approach, a prototype ultraviolet-visible-near infrared (348 to 910 nm) instrument was designed, fully assembled, characterized, and field tested. Our results demonstrate that this prototype ARCSTONE instrument provides a dynamic range larger than  $10^6$ , which is necessary to directly measure both the solar and lunar signals, and suggest uncertainties better than 0.5% ( $k = 1$ ) in measuring lunar spectra can be achieved under proper operational scenarios. We present the design, characterization, and proof-of-concept field-test of the ARCSTONE instrument prototype.

© The Authors. Published by SPIE under a Creative Commons Attribution 4.0 International License. Distribution or reproduction of this work in whole or in part requires full attribution of the original publication, including its DOI. [DOI: [10.1117/1.JRS.17.044508](https://doi.org/10.1117/1.JRS.17.044508)]

**Keywords:** lunar calibration; lunar reflectance; hyperspectral remote sensing; accuracy

Paper 230158G received Apr. 7, 2023; revised Sep. 15, 2023; accepted Oct. 12, 2023; published Nov. 1, 2023.

## 1 Introduction

Calibration accuracy and repeatability are key on-orbit performance metrics for Earth-observing sensors. The challenge is well-recognized by the science community, both nationally and internationally. The accuracy and consistency of measurements across multiple spaceborne instruments in low-Earth and geostationary orbits (LEO and GEO, respectively) are directly connected to the

\*Address all correspondence to Hans Courier, [courrier@resonon.com](mailto:courrier@resonon.com)

information content and scientific understanding from observing complex systems, such as the Earth's climate. Recent results have demonstrated the quantitative impacts of observational accuracy on the retrieved science parameters and the ability to detect trends for several essential climate variables, some examples of which are: the Earth's radiation budget, sea level and sea-surface temperatures, ice extent and ice-mass loss, cloud radiative forcing, and long-term trends in cloud parameters.<sup>1,2</sup> Accurate long-term calibrations of Earth-viewing spaceborne sensors have long been a challenge at reflected solar wavelengths. On-board optics and calibration devices can change during launch and suffer long-term degradation from exposure to a harsh space environment and radiation damage. Vicarious calibrations, using ground-targets having known reflectances, provide limited accuracy due to the variances introduced by observing through the Earth's atmosphere. Therefore, the use of an exoatmospheric calibration source within an instrument's dynamic range has the potential to be superior to traditional calibration approaches.

The Moon can be an ideal target for on-orbit calibration of Earth-viewing instruments, as the lunar surface is intrinsically stable over millennia, the lunar disk is of comparable brightness to Earth scenes, and the Moon is regularly visible to satellite-based instruments with no intervening atmosphere.<sup>3,4</sup> Regular lunar observations are currently implemented in support of long-term radiometric stability monitoring for the MODerate resolution Imaging Spectroradiometer (MODIS) and Visible Infrared Imaging Radiometer Suite (VIIRS) instruments.<sup>5,6</sup> A system to use the lunar irradiance as a calibration reference has been developed (i.e., the lunar irradiance model developed by the Robotic Lunar Observatory Project [ROLO])<sup>3,4</sup> and successfully applied to evaluate relative sensor response changes with subpercent precision, e.g., the Sea-viewing Wide Field-of-view Sensor (SeaWiFS).<sup>7</sup> But the Moon is not currently used for absolute calibration because uncertainties in the lunar calibration reference are too high, being at the ~5% to 10% levels.<sup>4</sup>

The radiometric quantity typically used for lunar calibration is the spatially integrated spectral irradiance.<sup>3</sup> This radiometric quantity can be generated for any observations of the Moon taken from LEO or GEO using an analytic model developed from extensive lunar measurements. The invariant nature of the Moon's surface reflectance means such a model can produce reference irradiances corresponding to observations of the Moon acquired at any time, including in the past. Improvements to this model can improve calibrations of past, current, and future on-orbit Earth-observing satellite instruments.

Improving the accuracy of the lunar calibration system requires collecting a new set of high-accuracy measurements to use as a basis for modeling. Recent projects that have been collecting lunar irradiance measurements include the Airborne Lunar Spectral Irradiance (air-LUSI) instrument flown on the ER2 platform<sup>8,9</sup> and photometer instruments operated at Izaña Atmospheric Observatory and Teide Peak, Tenerife, Canary Islands, supporting development of the lunar irradiance model of ESA (LIME).<sup>10</sup> Measurements are planned for the ground-based LUSI instrument at Mauna Loa Observatory (MLO-LUSI). The ground-based projects obtain high-quality lunar irradiance measurements at high temporal sampling, but a disadvantage of this method is that the necessary atmospheric corrections can limit overall accuracy to a few percent. Air-LUSI can achieve subpercent measurement uncertainties by flying above 95% of the Earth's atmosphere but at limited temporal sampling imposed by the airborne platform. However, both subpercent uncertainties and daily sample rates are achievable from measurements above the Earth's atmosphere taken from a satellite platform. This is the motivation and objective of the NASA ARCSTONE spaceflight project (Fig. 1).

## 2 ARCSTONE Instrument

### 2.1 ARCSTONE Concept

The ARCSTONE project intends to acquire on-orbit calibration measurements of the lunar spectral reflectance with 4-nm sampling over the 350 to 2300 nm spectral range with a combined uncertainty better than 0.5% ( $k = 1$ ) for Sun–Moon–ARCSTONE angles (i.e., lunar phase angles) up to  $\pm 90^\circ$ . This spectral range is designed to overlap with that of most Earth viewing sensors. To obtain high-accuracy lunar reflectance data to improve on-orbit intercalibrations, the 4-nm spectral sampling interval is selected to focus on maximizing signal retrievals following the analysis by Wu et al.<sup>11</sup> for solar spectral reflectance. The lunar reflectance is determined from direct measurements of the spatially integrated solar and lunar disks using the same set of

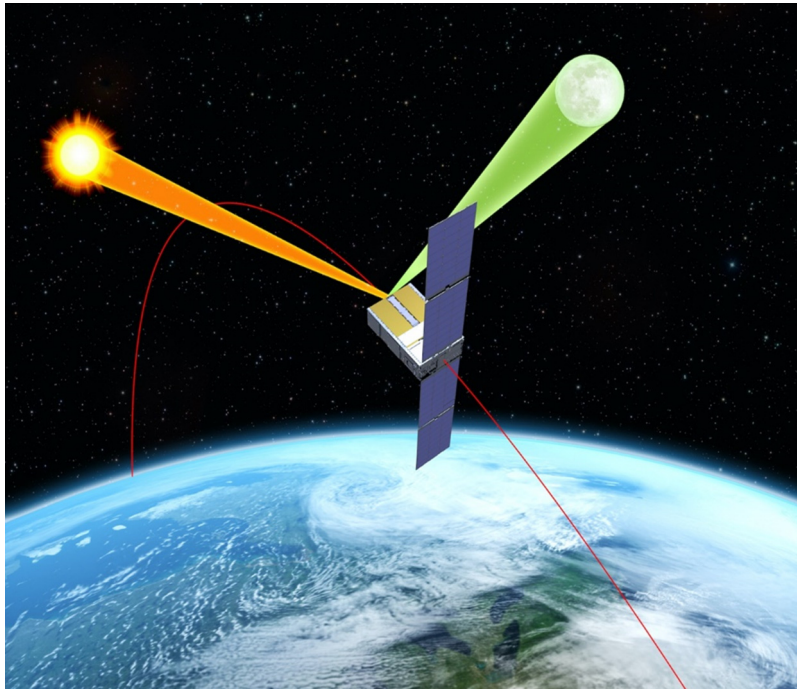


**Fig. 1** Conceptual illustration of the ARCSTONE instrument, the objective of which is to determine the lunar spectral reflectance from space with high accuracy by measuring irradiances from the Sun and Moon directly from a 6U CubeSat. (spacecraft bus image courtesy Blue Canyon Technologies).

spectrally dispersing optics. The ratios of the lunar to solar signals give the spectrally resolved lunar reflectances. These can be converted to spectral lunar irradiances via the independently known (from other NASA assets) SI-traceable spectral solar irradiance (SSI), essentially using the Sun as the ARCSTONE's on-orbit calibration source in much the same way that the NASA's CLimate Absolute Radiance and REfractivity Observatory (CLARREO) HyperSpectral Imager for Climate Science (HySICS) instrument does.<sup>12</sup> As with the HySICS, the Solar-to-Lunar cross calibration approach of this common-optics design allows long-term degradation of the ARCSTONE optics to be largely ignored since the lunar reflectance is determined using temporally close solar and lunar measurements.

Three major challenges of the ARCSTONE project include as follows:

1. measuring the large difference in signal strength between solar and lunar signals using the same optical system
2. achieving the needed 0.5 % uncertainties in lunar reflectances
3. incorporating the instrument on a small satellite.

The prototype instrument described in this paper focuses on addressing the first and second challenges. The final challenge drives an ARCSTONE instrument design that uses the same optics for spatially integrated measurements of both the Sun and Moon, which is possible because the two targets have nearly identical and small ( $\sim 0.5$  deg) spatial extents when viewed from low-Earth orbit. The small field of view from having nearly collimated incoming signals enables a slit-less spectrograph design which permits the signal from the entire solar or lunar spatial extent to be captured in a single frame. Beam-expansion fore-optics decrease the field angles incident on the back-end optics effectively demagnifying the spectral projection of the Solar or Lunar signal to fit within a single  $\sim 4$  nm bandpass spectral channel.

The primary challenge, that of signal strengths differing by  $\sim 10^6$ , is met by varying the instrument detector's integration time, and thus the acquired signal level, over several orders of magnitude while well-characterized detector linearity accounts for the remainder of the signal-strength differences. The maximum signal differences that could realistically be measured by

available focal-plane-array (FPA) detectors when varying integration times between the lunar and solar measurements were estimated to be  $\sim 10^4$ . Selecting the ARCSTONE spectrometer’s input aperture size to yield a solar signal close to the FPA’s pixel full-well depth results in lunar signal measurements  $\sim 10^2$  below the pixel full-well depth. This results in relatively poor signal-to-noise ratios (SNRs) for a single pixel; however, this problem is addressed by averaging multiple single-pixel measurements. More specifically, the instrument is designed with no optical power along one axis, and therefore every pixel of the two-dimensional FPA along this axis can be interpreted as an independent measurement. Averaging the pixels from each column of spectral data increases the SNR by approximately the square root of the number of pixels, which is sufficient to achieve uncertainties of  $<0.5\%$ .

The ARCSTONE project initially began as two separate modules, one utilizing a silicon CMOS detector and the other designed around a Mercury Cadmium Telluride (MCT) integrated detector cooler assembly. The resulting prototype instruments have spectral ranges of 348 to 910 nm for the ultraviolet-visible-near infrared (UV/VNIR) and 870 to 2300 nm for the short-wave infrared (SWIR), respectively. Individually, both prototype UV/VNIR and SWIR instruments are compatible with meeting challenges 1 and 3 noted above. However, the reduced complexity involved with deploying, collecting, and analyzing data from a single instrument led subsequent iterations of the ARCSTONE project to combine the spectral ranges of the two modules into a single, full spectral range (FSR) instrument. This follow-on FSR instrument is also designed around a small form factor and single, filter-less optical pathway for solar to lunar ratio measurements, while the “extended” spectral range (350 to 2300 nm) is achieved using a thinned-array MCT camera. (The FSR instrument iteration has demonstrated the desired 0.5% lunar-reflectance uncertainties over the 350 to 2300 nm range; further reporting on this instrument is planned for a later date.)

During early development of the FSR instrument, a characterization of the prototype UV/VNIR module was performed to inform continuing work and improvements incorporated into the FSR instrument iteration. The UV/VNIR module analyses and characterization are reported herein to establish a framework for meeting the three challenges listed above with the flight version of the FSR instrument.

## 2.2 ARCSTONE UV/VNIR Prototype Instrument Optical Design

Table 1 shows key optical design parameters of the UV/VNIR module, whereas a Zemax rendition of the module is provided in Fig. 2. In the system illustrated in Fig. 2, incoming solar or lunar radiation passes through a narrow rectangular cover window and entrance opening. The cover window protects the optics from UV rays, and the entrance opening serves as a baffle. After passing through the entrance opening, the incoming quasicollimated beam is expanded by a factor of 29 times by a pair of cylindrically symmetric mirrors labeled mirror 1 and mirror 2 (i.e., the beam expander). After this beam expansion, the incoming radiation passes through the system aperture stop, which applies in the spectral axis only. There is no optical power along the orthogonal axis, and the aperture stop for this nonpowered axis is at the image plane. After the

**Table 1** Select optical design characteristics of the ARCSTONE UV/VNIR module.

Property	Value
Waveband	348 to 910 nm
Focal plane array	Si, 1920 × 1080 pixels
Pixel size	7.4 μm (square)
FOV	0.6 deg
F-number	2.2
Spectral channels	147
Spectral sampling (channel)	3.83 nm

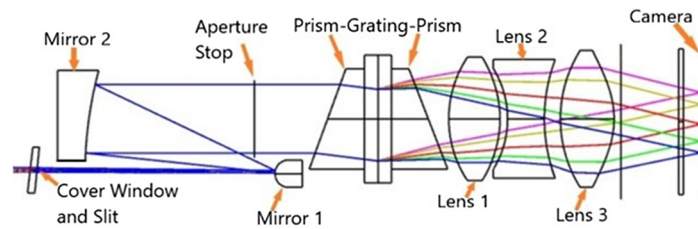


**Fig. 2** Zemax layout of the UV/VNIR module showing the spectral axis. There is no optical power along the orthogonal axis (into/out of the page) of the instrument.

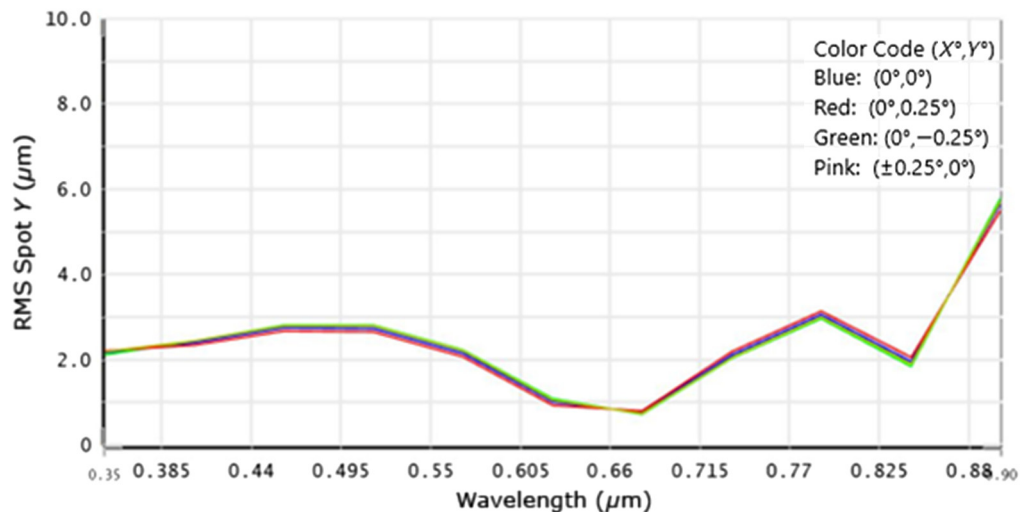


**Fig. 3** RMS line width as a function of wavelength for the ARCSTONE UV/VNIR instrument. RMS spot size in the instrument spectral axis is indicated by the Y axis in the plot.

system's spectral aperture stop, a prism-grating-prism (PGP) unit disperses the incoming light, and three cylindrical optics, labeled lenses 1 to 3, are used to form one dimensional "line" images on the FPA.

The nominal performance of the system can be characterized, in part, using a line spread function. The modeled root-mean-square (RMS) linewidth as a function of wavelength is shown in Fig. 3. The four different curves in Fig. 3 represent (1) the axial field, (2) 0.25 deg from the axial field along the nonpowered axis, (3) 0.25 deg from the axial field along the spectral axis, and (4) -0.25 deg from the axial field along the spectral axis. These fields thus represent the center and three edges of the full Moon or Sun. The four curves are nearly identical, indicating that the RMS linewidth of the system has very little dependence on field angle, which is a consequence of the instrument's beam expander. Similarly, the two classic grating distortions, smile and keystone, are not problematic in this system. Smile is small because the field angles of the Sun and Moon are small. Keystone is zero because light is nearly collimated along the nonpowered axis and the aperture stop for the nonpowered axis is at the image plane.

### 2.3 ARCSTONE Instrument Mechanical Design

Both instruments are designed in a modular fashion, consisting of a front barrel, a central barrel, a rear barrel, and the imager mount. This method allows for finding and mitigating any issues in the fabrication, assembly, and alignment before that error can propagate through to the final assembly. Mirror 2 is an acylindrical mirror with third-, fourth-, and fifth-order asphericity terms that is single-point diamond turned onto an aluminum substrate. In addition, a surface roughness of  $<40 \text{ \AA}$  RMS is also required for mirror 2 to meet the desired 4 nm spectral linewidth performance criterion. The mounting flexures for mirror 1 (rod mirror), kinematic mounting springs for the PGP, all internal baffles, and all fasteners are fabricated from stainless steel. Rulon J (a PTFE-filled bearing material) is used between lens 1 and lens 2 to athermalize the preload in that

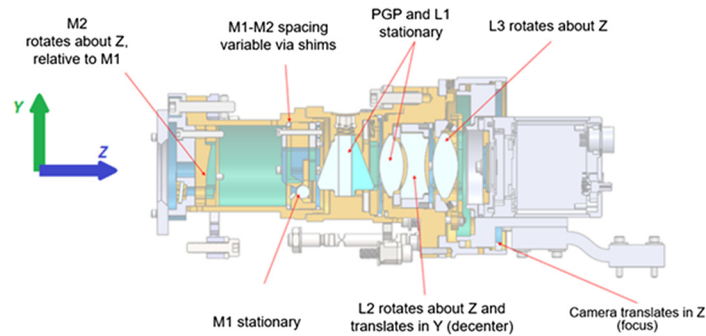


**Fig. 4** Mechanical design of the UV/VNIR instrument with degrees of freedom indicated.

lens stack. Flexures fabricated from 17-4PH stainless steel thermally isolate the optic train from the mounting fixture and also prevent over constraint of and stress introduction into the optic train.

The UV/VNIR instrument features a silicon-based sensor mounted in a barrel structure at the aft end of the spectrometer. This design is engineered to meet all optical requirements with the minimum degrees of freedom needed for alignment, as indicated in Fig. 4. No thermal metering is used, as a “snubbing rod” constrains motion along the degree of freedom created by the mounting flexures.

#### 2.4 ARCSTONE Instrument Structural/Thermal Analysis

Structural thermal optical performance analyses were performed to estimate the expected optical performance after launch and deployment in low-Earth orbit for the optomechanical model. For this analysis, two bracketing environments, a hot case (+53°C) and a cold case (−23°C), were identified from a preliminary on-orbit thermal analysis performed by NASA Langley Research Center. The thermal analysis was then performed for transient thermal environments to simulate a thermal vacuum chamber test. The optical performance was quantified by simulating the 587 nm RMS spectral linewidth for the cold case. Further details of the analysis and design changes made to minimize the effect of the thermal environment on the instrument’s performance are described in Ref. 13.

Random vibration was analyzed according to GSFC-STD-7000 (General Environmental Verification Standard)<sup>14</sup> Minimum workmanship levels (6.8 G RMS) to determine the structural survival of the instruments’ mounting flexures under launch loads. The instrument mounting flexures (see Fig. 5) are designed to isolate the barrel portion of the instrument from stresses that are applied through the mounting structure. Therefore, the barrel portion of the instrument

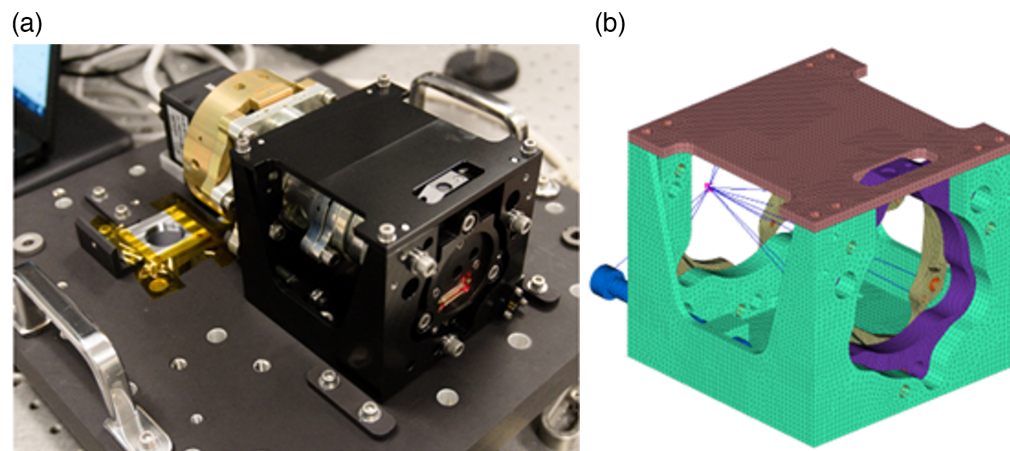


**Fig. 5** (a) The fully assembled UV-VNIR instrument. The mounting flexures are contained within the black anodized mounting structure that encompasses the front most portion of the instrument in center-left of the image. (b) FEM mesh on a model rendering of the UV/VNIR mounting structure and flexure assembly.

should only include very high-frequency modes and respond as a rigid body up to 2000 Hz. The random vibration FEMs included detailed representations of the instrument mounting components for stress recovery and a lumped mass representation of the barrel portion of the instrument [see Fig. 5(b)]. This lumped mass element included the mass, moments of inertia, and center of gravity of the barrel portion of each instrument to ensure the loads and resulting mode shapes of the flexures were accurately captured. Three-sigma stresses and forces throughout the mounting components were recovered and used to calculate strength margins of safety using the appropriate material strength allowables and factors of safety as specified by Ref. 14. Margins of safety for all bolted joints and pins were also calculated using NASA-STD-5020<sup>15</sup> with the appropriate applied preloads, material allowables, and factors of safety from Ref. 14. This analysis determined that all margins of safety for both instruments are positive for random vibration.

### 3 Characterization and Results

ARCSTONE calibrations and characterizations were performed at both the component and system levels. Component-level calibrations primarily focused on detector calibrations and included characterizations of read noise, dark current, uniformity, gain, thermal sensitivity, linearity, and dynamic range. System-level calibrations and characterizations, done at the assembled-instrument stage, involved sensitivity to stray light, pointing, and polarization; spectral dispersion; response to thermal fluctuations; and efficiency across the spectral range. As only the UV/VNIR instrument was assembled to this level, only results from it are described here, although the component-level results from both FPAs were obtained.

#### 3.1 ARCSTONE Component-Level (Detector) Calibrations

The UV/VNIR detector is a 14-bit Imperx B1923 focal-plane array. Using a preamplifier gain setting of  $-3$  and an analog gain setting of 50 on the supplied focal plane electronics (FPE), the unit is characterized for shutter timing and sensor linearity, read noise, dark current versus temperature, and gain. The integration times span the range from  $2 \mu\text{s}$  to 16 sec, providing nearly seven orders of magnitude of dynamic range, which is sufficient for the ARCSTONE solar and lunar measurements. Characterization results are summarized in Table 2.

A characteristic photon-transfer curve is shown in Fig. 6. The read noise can be inferred from the vertical-axis intersection, whereas gain is determined by a linear fit to the higher-signal portion of Fig. 6. The unit shows an increase in noise manifesting as a bump in the photon-transfer curve between  $\sim 1$  and  $\sim 100$  data numbers (DN) that is not understood. This bump is fitted and removed to obtain the read noise and gain values.

Dark current is characterized with signal readings from a series of integration times (25 logarithmically spaced times from  $2 \mu\text{s}$  to 16 s) with no input light on the array. Performing these tests in a thermal chamber characterized the FPA's dark current as a function of temperature from  $18^\circ\text{C}$  to  $57^\circ\text{C}$ , as shown in Fig. 7. Dark current is nearly at a minimum at ambient temperatures, so no FPA cooling is required for this device. The average dark current at an FPA temperature of  $40^\circ\text{C}$  is  $\sim 1 \text{ e}^- \text{ s}^{-1} \text{ pixel}^{-1}$ . At this rate, the single-pixel uncertainty due to the shot noise of dark current at the full 16-s integration time would be  $<0.1\%$  for signals above 1740 DN.

**Table 2** UV/VNIR FPA characterization results.

Parameter	Value
Read noise	2.8 DN
Dark current	$0.25 \text{ e}^- \text{ s}^{-1}$ at $20^\circ\text{C}$
Bad pixels	472 (0.02% of array)
Gain (averaged over all pixels)	$2.34 \text{ e}^- \text{ DN}^{-1}$
Shutter-timing linearity	$<4 \times 10^{-8}$ over $10^7$ dynamic range
Sensor linearity	$<2000$ ppm up to 80% of full well

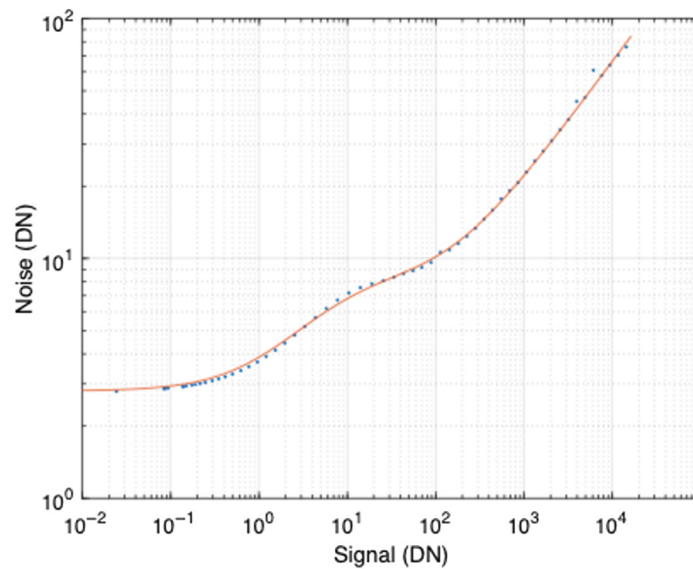


**Fig. 6** This photon-transfer curve spanning six orders of magnitude gives the FPA’s read noise and gain. The odd bump between ~1 and ~100 DNs is not understood but is reproducible and fitted to enable the characterizations.

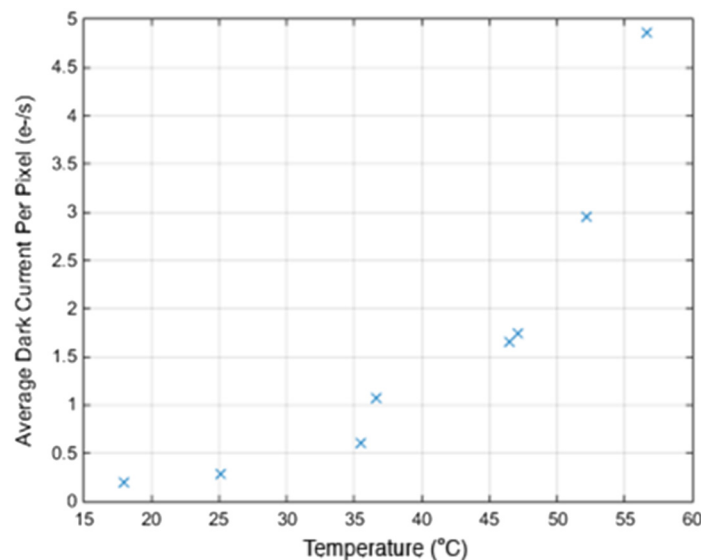


**Fig. 7** Dark current as a function of temperature indicates that ambient-temperature operations are near the achievable minimum.

Electronic shutter-timing linearity is characterized using a high-frequency signal analyzer and measuring the linearity of the FPE pulses that control the electronic FPA shutter. No significant nonlinearities (at the  $4 \times 10^{-8}$  level) in electronic shutter timing are found across the range of integration times. This is largely as expected for electrical-signal timings.

The FPA itself, however, is expected to have nonlinearities, particularly at high-signal levels. Sensor linearity calibrations are performed via two independent means: varying the integration times at a nearly constant signal level and varying the signal level at a constant integration time with that signal level being measured by a National Institute of Standards and Technology (NIST)-calibrated reference photodiode monitor with corrections applied for photoresponsivity. Results showed consistency at the 0.35% level. Deviations from linearity for the calibration method of varying signal levels are shown in Fig. 8.

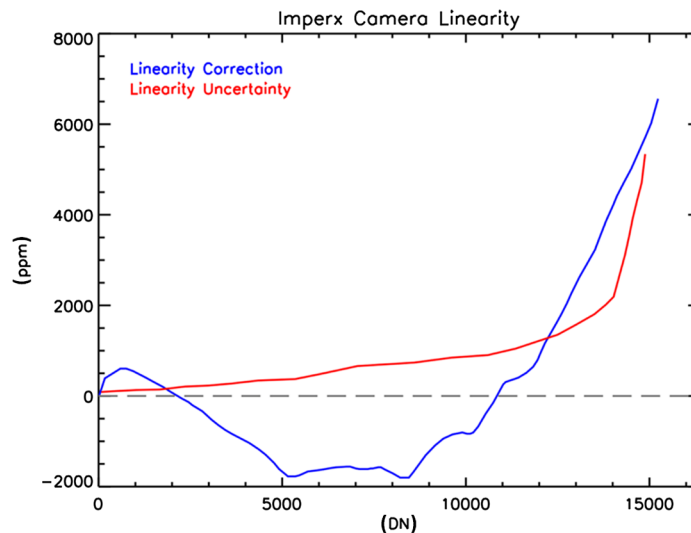


**Fig. 8** Residuals from linearity across the read-out dynamic range are generally within 2000 parts per million (ppm or  $10^{-4}\%$ ) of linear (blue curve). Being reproducible, these can be calibrated out such that the uncertainties due to linearity corrections are  $<0.1\%$  across most of the dynamic range ( $<10,000$  DN) (red curve).

The detector did show 472 “misbehaving” pixels in the testing performed. Being a mere 0.02% of the array, these cause no restrictions on intended measurements.

The detector meets the component-level requirements for the intended ARCSTONE use. End-to-end system-level tests and additional field tests with the fully assembled instrument validate that it meets required uncertainties specified at this stage in the prototype-instrument demonstration effort, as described in Sec. 3.2.

Many of the FPA uncertainties, such as those from read noise, dark current, and shot noise, are type A (i.e., statistical), and thus can be reduced via repeated measurements, where such are possible. These uncertainties, relative to the signal itself, decrease monotonically with signal level, as expected. The primary type B (systematic) uncertainties for this instrument are due to nonlinearity corrections, which increase near the upper range of signal levels. A preliminary summary of the type A and B uncertainties as well as their combined uncertainty for a particular anticipated lunar-viewing configuration is shown in Fig. 9. From this plot, ideal signal values are

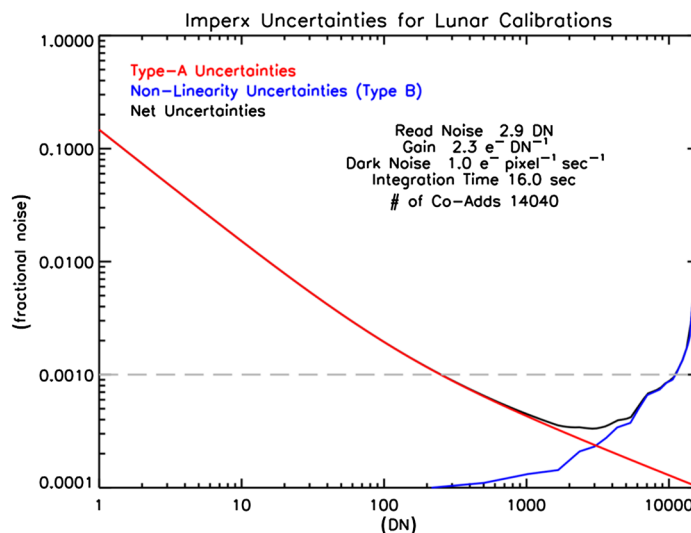


**Fig. 9** Expected uncertainties based on the component-level calibrations are shown as a function of signal (DN) for the UV/VNIR detector. The type A uncertainties benefit from multiple nonimaging-direction coadds for this representative example of a lunar measurement.

between 300 and 10,000 DN, where expected net uncertainties below 0.1% can be achieved. These signal levels can be achieved by selection of an appropriate integration time for any chosen source.

Overall, we find that the UV/VNIR instrument’s FPA is capable of the desired ARCSTONE measurement uncertainties given appropriate operating conditions and sufficient sampling.

### 3.2 ARCSTONE System-Level Characterizations

The completed UV/VNIR instrument was characterized for field of view, scatter, instrument line shape, throughput efficiency, polarization sensitivity, thermal response, optical alignment, and spectral dispersion. End-to-end field tests were completed to demonstrate the ARCSTONE instrument’s approach of acquiring both lunar and solar irradiances. An uncertainty budget gives estimates of the instrument’s accuracies in determining lunar irradiances based on the SI-traceable SSI.

#### 3.2.1 Spectral dispersion

Spectral accuracy and dispersion are characterized using a HgAr pen-ray lamp. A spline fit to the source’s known atomic emission lines and the measured locations on the FPA give good agreement. The full NIST Hg atomic line database is used in determining spectral lines from the pen-ray. Instrument wavelength-scale uncertainty combined with scene spectral variations give wavelength-dependent uncertainties that are greatest near spectral lines.

#### 3.2.2 Instrument line shape (and pointing sensitivity)

The ARCSTONE optical design (see Sec. 2.2) requires different rotation axis locations for pointing-sensitivity tilts in the two (nonpowered and spectral) orientations. Mounts were made for the lab testing of sensitivity to pointing to use the appropriate rotation axis for each orientation.

Instrument line shapes are determined at five wavelengths (382, 520, 642, 749, and 890 nm) using a fiber-coupled tunable laser feeding a collimator. Two-axis pointing maps are acquired over an incidence-angle range of  $\pm 0.75$  deg, providing 60,000 images from which pointing sensitivities are determined. An example of these is shown in Fig. 10. The pointing sensitivity in the spectral dimension (the more sensitive of the two) is found to be  $\sim 0.016$  nm/arc min).

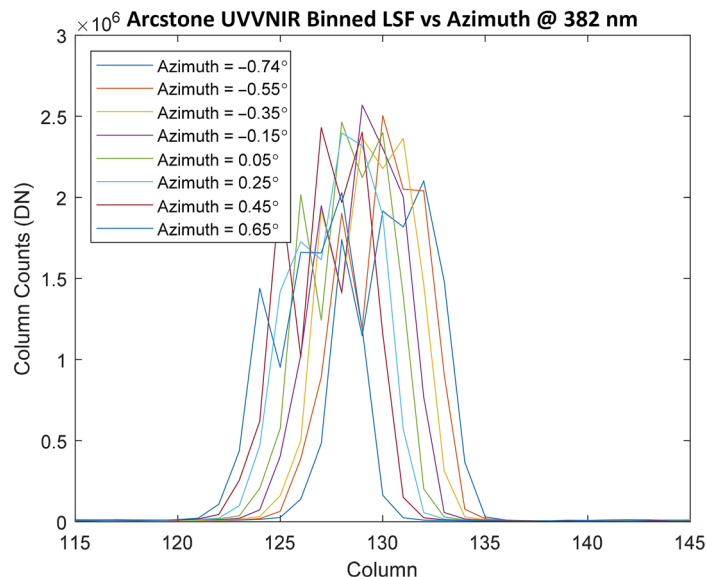


**Fig. 10** Instrument line shape was measured as a function of pointing, from which spectral sensitivity across the field of view can be determined. This plot shows the instrument line shape for eight incidence angles in the spectral dimension, which is the more sensitive of the two orientations.

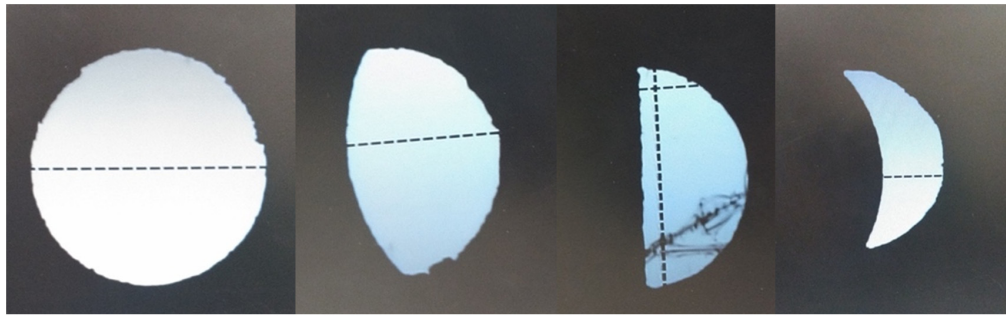


**Fig. 11** Lab measurements with different lunar crescent shapes helped estimate the instrument's sensitivity to this 0.5 deg extended source. (The cutouts used are  $\sim 1$  mm tall.)

Sensitivity to pointing is particularly important for the asymmetric optics in the ARCSTONE design, as a pointing offset in the spectral direction will linearly map to a spectral shift. The beam expander at the front of the instrument (see Sec. 2.2) reduces this sensitivity by  $\sim 29\times$  but cannot eliminate it. Since the Moon is asymmetric in shape except at 0 deg phase (i.e., full moon), the  $\sim 0.5$  deg extended lunar crescent will manifest as different spectral shifts for different portions of the crescent. These were modeled using a nonsequential Zemax model of the instrument for various lunar shapes. The model-based results are also verified with lab measurements of the instrument sensitivity to pointing as well as using cutout shapes of lunar crescents which are rotated to different orientations for testing (see Fig. 11).

### 3.2.3 Field-of-view (stray light)

Stray light was measured via large off-axis measurements. No significant stray light was found, meaning light from the Earth's disk and the Sun were determined to not be an issue.

### 3.2.4 Polarization

Polarization sensitivity is determined using a rotating half-wave plate to vary the incident polarization state. The instrument demonstrates a diattenuation of  $\sim 0.025$  at 633 nm.

### 3.2.5 Lunar-irradiance field test (dynamic range)

A ground-based field test of the instrument gave an end-to-end demonstration of the as-intended method of calibrating the lunar irradiance from the known SSI. These ground-based measurements are affected by atmospheric scatter and losses; high radiometric accuracies were not expected from this method of demonstration. The prototype-instrument field-test results, shown in Fig. 12, demonstrate that the instrument can acquire solar and lunar irradiances despite the  $>10^6$  difference in signal levels between the two sources. The lunar measurements were acquired one day after full moon. Thin atmospheric haze reduced the full lunar signal somewhat. The solar measurements were acquired four days later, so are expectedly under very different atmospheric conditions. The measured ratio shown in Fig. 12 is presented as a representation or proxy for reflectance here, but the objective is not to demonstrate an actual measurement of lunar reflectance.

### 3.2.6 Uncertainty summary

An instrument uncertainty budget was created as a function of wavelength for the ARCSTONE solar/lunar ratio measurements using this UV/VNIR instrument. Component-level contributions include effects from read noise, signal and dark-current shot noise, quantization noise, and non-linearities, many of which are described above. Those contribute to each image but can be reduced via multiple-frame co-adds, as suggested by an observing sequence in Fig. 9. Images of the Sun, Moon, and dark space require several such multiple-frame observations that will vary

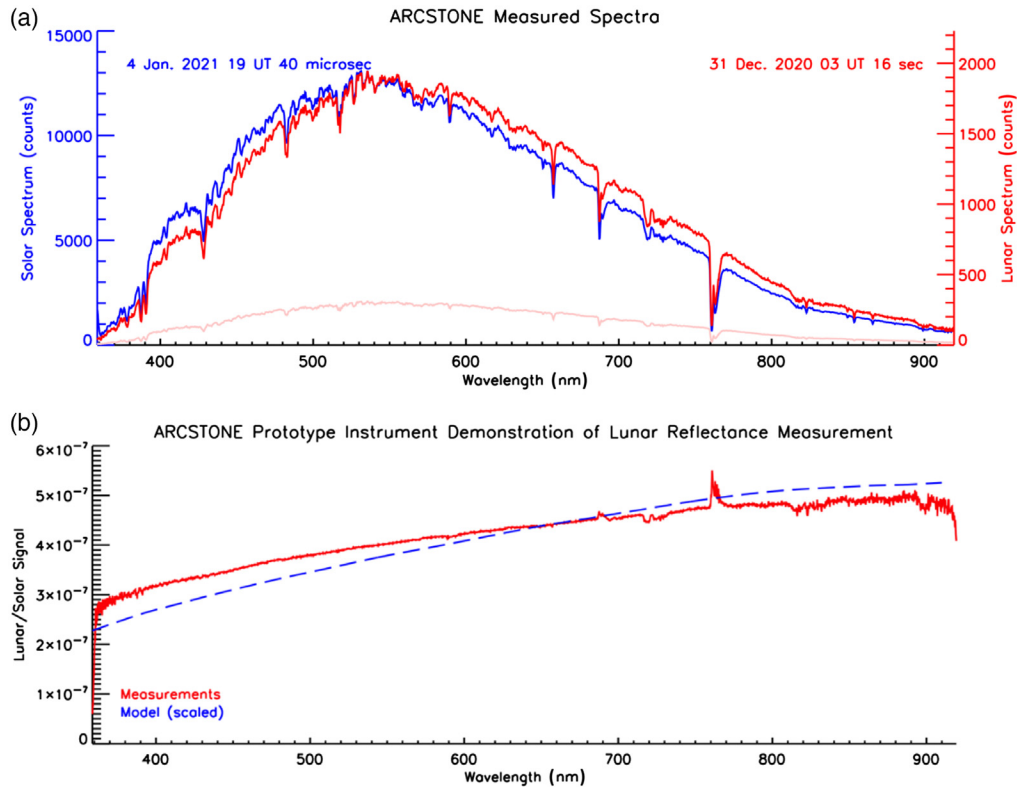


**Fig. 12** (a) Solar (blue) and lunar (red) spectral measurements were acquired using different integration times for each. The faint red curve gives the lunar measurements on the same scale as the solar measurements. (b) The ratio between the lunar and solar spectral measurements (red) is compared with a model (dashed blue) based on known lunar-sample reflectance as a function of wavelength. This verifies that the instrument can measure lunar reflectances that are  $<10^{-6}$ , achieving the needed dynamic range.

with lunar phase to reduce uncertainties to desired levels. These are indicated by the solar and lunar contribution plots in Fig. 13. The dark-corrected solar (red) and lunar (blue) signals can then be ratioed, giving the total uncertainty (black) for the lunar-signal measurement. The net results shown in Fig. 13 suggest promise for achieving the desired uncertainties across nearly the entire spectral range.

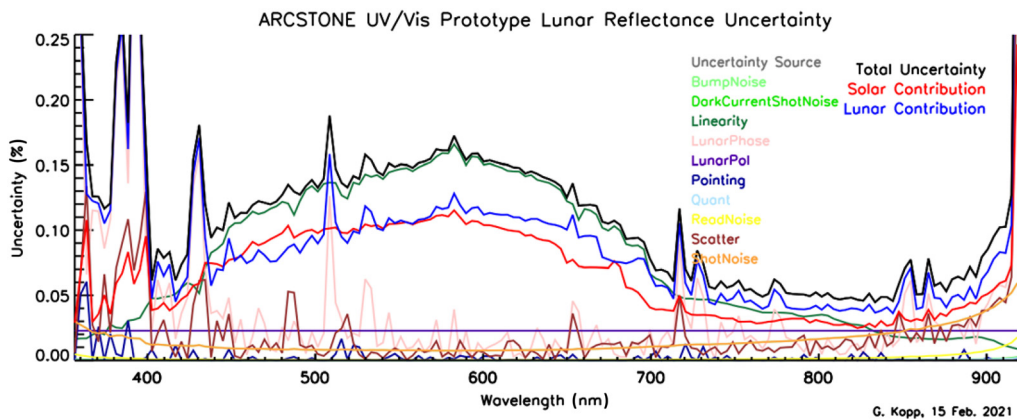


**Fig. 13** Uncertainties from several contributing effects described in the text are characterized as a function of wavelength. The expected combination of these for a full solar/lunar ratio comparison (black curve) indicates measurement capability with uncertainties of  $<0.2\%$  across most of the desired spectral range, greatly exceeding intended capabilities.

## 4 Summary and Conclusions

The ARCSTONE concept and a prototype instrument sensitive to UV/VNIR wavelengths are described. Extensive modeling and testing of instrument components and the full UV/VNIR instrument are described, and the results are presented. A proof-of-concept field test, shown in Fig. 12, demonstrates the ARCSTONE UV/VNIR instrument's ability to measure both the Sun and Moon using the same optical system despite their  $10^6$  signal-level differences. The expected combined uncertainties for the UV/VNIR instrument, shown in Fig. 13, are lower than the 0.5% uncertainty goal across most of the instrument's spectral range.

The prototype UV/VNIR ARCSTONE instrument laid the groundwork for a second-generation ARCSTONE instrument that spans the FSR from 350 to 2300 nm. A prototype FSR ARCSTONE instrument has been designed, fabricated, and tested.<sup>16</sup> A flight iteration of the ARCSTONE FSR instrument is currently being developed for a technology demonstration in low-Earth orbit with funding from NASA's In space Validation of Earth Science Technologies (InVEST) program. The anticipated ARCSTONE launch is planned for the mid-2025 timeframe through the NASA CubeSat Launch Initiative (CSLI) program.<sup>17</sup>

---

### Code, Data, and Materials Availability

Open-source code development and dissemination to the public is not included in the ARCSTONE project for the instrument described herein; any interested parties are welcome to contact the authors for further information.

### Acknowledgments

This work was funded by the NASA SBIR Program (Project Nos. 80NSSC17C0004 and 80NSSC19C0167) and the NASA Earth Science Technology Office Instrument Incubator Program (Project No. IIP-QRS-16-0018). The authors would like to acknowledge support from the NASA Langley Research Center Science Directorate. The authors have no conflicts of interest to disclose.

### References

1. B. A. Wielicki et al., "Achieving climate change absolute accuracy in orbit," *Bull. Am. Meteor. Soc.* **94**, 1519–1539 (2013).
2. Y. L. Shea et al., "Quantifying the dependence of satellite cloud retrievals on changes in instrument calibration," *J. Clim.* **30**(17), 6959–6976 (2017).
3. H. H. Kieffer and T. C. Stone, "The spectral irradiance of the Moon," *Astron. J.* **129**, 2887–2901 (2005).
4. T. C. Stone et al., "The moon as a climate-quality radiometric calibration reference," *Remote Sens.* **12**, 1837 (2020).
5. J.-Q. Sun et al., "MODIS reflective solar bands on-orbit lunar calibration," *IEEE Trans. Geosci. Remote Sens.* **45**(7), 2383–2393 (2007).
6. X. Xiong et al., "Lunar calibration and performance for S-NPP VIIRS reflective solar bands," *IEEE Trans. Geosci. Remote Sens.* **54**(2), 1052–1061 (2016).
7. R. E. Eplee et al., "On orbit calibration of SeaWiFS," *Appl. Opt.* **51**(36), 8702–8730 (2012).
8. J. Woodward et al., "Measurements of absolute, SI-traceable lunar irradiance with the airborne lunar spectral irradiance (air-LUSI) instrument," *Metrologia* **59**(3), 034001 (2022).
9. S. Grantham et al., "The irradiance instrument subsystem (IRIS) on the Airborne-Lunar Spectral Irradiance (air-LUSI) instrument," *Meas. Sci. Technol.* **33**(6), 065021 (2022).
10. C. Toledano et al., "LIME: lunar irradiance model of ESA, a new tool for the absolute radiometric calibration using the Moon," *EGU sphere* (2023).
11. A. Wu et al., "Sensitivity of intercalibration uncertainty of the CLARREO reflected solar spectrometer features," *IEEE Trans. Geosci. Remote Sens.* **53**(9), 4741–4751 (2015).
12. G. Kopp et al., "Radiometric flight results from the hyperspectral imager for climate science (HySICS)," *Geosci. Instrum. Method Data Syst.* **6**, 169–191 (2017).
13. C. Buleri et al., "Structural, thermal, and optical performance (STOP) analysis of the NASA ARCSTONE instruments," *Proc. SPIE* **10925**, 1092503 (2019).
14. NASA Standard, "General Environmental Verification Standard (GEVS) for GSFC Flight Programs and Projects," GSFC-STD-7000, Version B, April 28 (2021), <https://standards.nasa.gov/standard/GSFC/GSFC-STD-7000>.

15. NASA Standard, "Requirements for Threaded Fastening Systems in Spaceflight Hardware," NASA-STD-5020, Version B, August 6 (2021), <https://standards.nasa.gov/standard/NASA/NASA-STD-5020>.
16. R. Swanson et al., "The ARCSTONE project to calibrate lunar reflectance," in *IEEE Aerosp. Conf.*, 7-14 March 2020, Big Sky, MT, USA, pp. 1–10 (2020).
17. J. Costa, Ed., "NASA CubeSat Launch Initiative (CSLI)," October 2 (2023), <https://www.nasa.gov/kennedy/launch-services-program/cubesat-launch-initiative/>.

**Hans Courrier** received his MS degree and PhD in physics from Montana State University in 2019, where his primary research focused on extreme ultraviolet spectroscopy and imagery of the solar atmosphere. He was a key team member in two successful launches of the MOSES solar sounding rocket instrument and performed the detailed optical design analysis for a new rocketborne instrument called ESIS. He is also experienced in science operations and data analysis for the NASA IRIS Small Explorer mission. He joined Resonon and the Bozeman photonics industry in the spring of 2018, where he began work on radiometric modeling and assembly and alignment of the ARCSTONE UV/VNIR, SWIR, and FSR instruments. He is currently Principal Investigator on a NASA SBIR that seeks to develop a low-cost hyperspectral imager for high-quality measurements of aquatic reflectances.

**Constantine Lukashin** received his MS degree in nuclear physics and engineering from Saint Petersburg Polytechnic University, Saint Petersburg, Russia, and his PhD in physics from Virginia Polytechnic Institute and State University, Blacksburg, Virginia, United States. He participated in nuclear and high-energy particle physics experiments from 1990 to 2001, working at national accelerator facilities in Russia, Italy, France, and the United States. In 2001, he joined the NASA CERES team as a research scientist for the development and validation of the angular distribution models (ADM). As a member of the CERES team, he developed an artificial neural network approach for reproducing ADMs in the absence of coincident imager observations and as a working group lead developed an intercalibration approach for CLARREO and CLARREO Pathfinder missions. He is currently a research physical scientist at the NASA Langley Research Center, Hampton, Virginia, United States, where he is the Principal Investigator of the ARCSTONE InVEST project for accurate calibration of lunar spectral reflectance from space.

**Christine Buleri** received her BS degree in mechanical engineering from Boston University and her MS degree in structural engineering from University of California San Diego, with coursework focused on structural dynamics and nonlinear simulations. She has 19 years of industry experience performing detailed FEA for optical systems including telescopes, payloads, and instruments for ground, air, and space. Since joining Quartus in 2004, she helped to develop many in-house tools for integrated optomechanical analysis including predictions for STOP, jitter, WFE, and stress using both linear and nonlinear techniques.

**Greg Kopp** received his BS degree in physics from California Institute of Technology and his PhD in physics from Stanford University. He has worked at the NASA/Ames Research Center, National Solar Observatory, Meadowlark Optics, and Ball Aerospace. He is currently a Senior Research Scientist IV of the Laboratory for Atmospheric and Space Physics (LASP) at the University of Colorado, where he initiated and lead development of the CLARREO HySICS instrument, for which he is instrument Principal Investigator at LASP. He specializes in space-based radiometry and has been PI, Co-I, and/or instrument lead on SORCE, Glory, TCTE, and TSIS-1 missions or instruments. He is the LASP PI for the ARCSTONE.

Biographies of the other authors are not available.